

## Confined Phase Singularities Reveal the Spin-to-Orbital Angular Momentum Conversion of Sound Waves

Ludovic Alh  t  z<sup>1</sup>, Thomas Brunet<sup>1</sup>, Christophe Arist  gui, Olivier Poncelet<sup>1</sup>, and Diego Baresch<sup>1\*</sup>  
*Universit   Bordeaux, CNRS, Bordeaux INP, I2M, UMR 5295, F-33400 Talence, France*

 (Received 12 December 2022; accepted 1 August 2023; published 13 September 2023)

We identify an acoustic process in which the conversion of angular momentum between its spin and orbital form takes place. The interaction between an evanescent wave propagating at the interface of two immiscible fluids and an isolated droplet is considered. The elliptical motion of the fluid supporting the incident wave is associated with a simple state of spin angular momentum, a quantity recently introduced for acoustic waves in the literature. We experimentally observe that this field predominantly forces a directional wave transport circling the droplet’s interior, revealing the existence of confined phase singularities. The circulation of the phase, around a singular point, is characteristic of angular momentum in its orbital form, thereby demonstrating the conversion mechanism. The numerical and experimental observations presented in this Letter have implications for the fundamental understanding of the angular momentum of acoustic waves, and for applications such as particle manipulation with radiation forces or torques, acoustic sensing and imaging.

DOI: [10.1103/PhysRevLett.131.114001](https://doi.org/10.1103/PhysRevLett.131.114001)

It is widely accepted that the longitudinal nature of sound waves cannot provide for a spin angular momentum (AM) density in the supporting liquid or gas. Indeed, in the absence of an efficient transverse restoring mechanism, the motion of a lossless fluid carrying sound waves is often thought to remain exclusively aligned with the propagation direction, and therefore lacks the kind of rotational degrees of freedom that lead to spin AM. While this is easily verified for the ideal case of homogeneous plane waves, the actual fluid motion in, e.g., nonparaxial beams, interfering waves or surface waves is more complex, and the existence of a finite spin AM density has recently been suggested [1–4].

For light, in contrast, the separation of AM into a spin part associated with the circular transverse polarization of the electric field [5], and an orbital part associated with the spatial distribution of the phase [6] is well established and has been confirmed by several experiments two decades ago [7–9]. Nevertheless, a recent interest in these quantities in the context of highly structured or confined optical fields has revealed other intriguing properties of the AM of light, generically termed spin-orbit interactions, provided the full vectorial character of Maxwell’s equations is considered, comprising polarization components of the electric and magnetic fields pointing in the direction of propagation, transverse components of the spin AM density [10–12], conversion mechanisms between the two forms of AM [13,14], and interaction rules with quantum emitters [15,16].

In lossless fluids, longitudinal sound waves are frequently termed “pressure” or “scalar” waves, and the analysis of the

vectorial properties of the velocity field are generally overlooked, with the exception of a few reported seminal studies [17,18], and more recent accounts on polarization singularities and topological properties of sound [19,20]. In particular, this may explain why only AM in its orbital form, which arises from specific spatial phase properties of a scalar potential field, has been previously investigated in acoustic vortex beams [21–24]. Consequently, most accounts of “spinlike” states of sound, or spin-orbit interactions have been reported in artificial elastic structures [25–28]. For transverse elastic waves in crystals (phonons)—known to share several properties with light (photons) [29,30]—the experimental evidence of an existing spin AM is only very recent [31,32].

The renewed interest in the fundamental nature of the AM density of sound waves in simple fluids, with the recent proposition of its separation between well-defined orbital and spin components, calls for the development of experiments sensitive to both forms of AM through direct wave field measurements or the mechanical evidence of their transfer to matter [33,34].

Here, we identify a process by which the spin AM density of a propagating longitudinal sound wave is converted into AM in its orbital form. We characterize the interaction between an isolated fluid droplet and an incident evanescent (inhomogeneous) field. By exploiting minimally invasive and high resolution acoustic pressure measurements, we were able to map the spatial properties of the internal acoustic field. Our measurements reveal the emergence of wave fronts circulating around phase singularities confined in millimeter-sized resonant droplets.

The circulation of the wave's phase around singular points is a hallmark for orbital AM imparted to the fluid, which is found to coexist with a nontrivial spin AM density inside the droplet.

*Transverse spin density of the incident evanescent wave.*—In a lossless fluid of mass density  $\rho$ , the spin AM density of a sound wave was recently derived as [2–4]

$$\mathbf{s} = \frac{\rho}{2\omega} \text{Im}(\mathbf{v}^* \times \mathbf{v}) = \frac{1}{2\rho\omega^3} \text{Im}(\nabla p^* \times \nabla p), \quad (1)$$

where  $\mathbf{v}$  is the complex velocity field in an Eulerian description of the fluid motion,  $*$  denotes its complex conjugate,  $\text{Im}$  denotes the imaginary part, and Euler's linearized momentum equation,  $i\omega\rho\mathbf{v} = \nabla p$  was used for a monochromatic pressure field,  $p$ , varying in time,  $t$ , as  $e^{-i\omega t}$  with a frequency,  $f = \omega/2\pi$ . Evanescent plane waves are an example of inhomogeneous acoustic fields that give rise to a simple state of transverse spin AM [3]. They are plane wave solutions of the propagation equation obtained using a complex-valued wave vector  $\mathbf{k} = k_z\mathbf{e}_z + ik_x\mathbf{e}_x$ . The pressure field can be written as

$$p(x, z, t) = p_a e^{-\kappa x} e^{i(k_z z - \omega t)}, \quad (2)$$

where  $x$  denotes the vertical direction (unit vector  $\mathbf{e}_x$ ) along which the wave amplitude decays exponentially,  $z$  denotes the propagation direction (unit vector  $\mathbf{e}_z$ ), and  $p_a$  is a reference acoustic pressure amplitude (see Fig. 1). The solution is invariant in the  $y$  direction. The dispersion relation  $\mathbf{k} \cdot \mathbf{k} = k_z^2 - \kappa^2 = k^2$  relates the propagation wave

vector  $k_z$  to the spatial decay rate  $\kappa$  via the wave number  $k = \omega/c$ , where  $c$  is the speed of sound in the fluid. The local fluid displacement field is  $\mathbf{u} = i\omega^{-1}\mathbf{v}$ .

It is important to note that the wave field is longitudinal, i.e., the acoustic displacement vector  $\mathbf{u}$  and the wave vector  $\mathbf{k}$  are collinear. However, because  $\mathbf{k}$  is complex valued, a fluid particle initially located at a position  $\mathbf{x}_0$  will follow the displacement  $\mathbf{u}(\mathbf{x}_0)$  that locally describes an elliptical trajectory determined by the relative magnitude of  $k_z$  and  $\kappa$  [17,18]. Nevertheless, it is easy to verify that such a ‘‘polarization’’ of the fluid motion does not violate its fundamental irrotational nature ( $\nabla \times \mathbf{u} = \mathbf{0}$ ), schematically illustrated by the unchanged orientation of an isolated fluid ‘‘particle’’ in Fig. 1(d) during its one-period center-of-mass trajectory. The elliptical trajectory of the fluid motion is somewhat similar to the orbits observed for gravity water waves, for which a spin density has been introduced and recently measured [35,36].

To experimentally generate an evanescent acoustic wave, we designed a setup inspired by Refs. [37,38], that offers appropriate conditions to obtain the total internal reflection of an incident finite beam generated in medium (1) at the interface with medium (2) (Fig. 1(a), and Supplemental Material, Sec. I [39]). Critical reflection conditions are obtained by using a ‘‘slow’’ incident medium (1) having a low speed of sound relative to the ‘‘fast’’ transmission medium (2). We chose for medium (1) a fluorinated oil immiscible with water (Fluorinert FC-40), of mass density ( $\rho_1 = 1850 \text{ kg/m}^3$ ) and speed of sound,  $c_1 = 640 \text{ m/s}$  [44]. Medium (2) was a yield-stress gel prepared by mixing distilled water with a carbomer (Carbopol<sup>®</sup>). The incident angle  $\theta_i$  relative to the  $x$  direction was adjusted to exceed the critical angle  $\theta_c = \sin^{-1}(c_1/c_2) \sim 25^\circ$ . The instantaneous pressure variation could be mapped in three dimensions (3D) using a fiber optic hydrophone system (Precision Acoustics, UK). The fiber is  $100 \mu\text{m}$  in diameter, with a sensitive area of  $10 \mu\text{m}$  that defines our resolution. Wave packets of 5 to 10 acoustic cycles were generated by the transducer (central frequency of  $f = 1 \text{ MHz}$ , with a 60% bandwidth) and sent toward the interface. The amplitude decay in the  $x$  direction was obtained from the Fourier transform (analyzed at 1 MHz),  $\tilde{p}$ , applied to the time-dependent pressure field as shown in Fig. 1(b) (dots). The decay length was obtained from an exponential fit of the data points (plain blue curve), and estimated to be  $1/\kappa \sim 0.64 \text{ mm}$ . The red data point was supposed to lie at the interface  $x = 0$  and excluded from the fit. Its value was used as the reference pressure  $p_a = 50 \pm 7 \text{ kPa}$ .

A direct quantification of the spin density can be obtained from the local estimate of the acoustic velocity field from discrete pressure measurements [see Eq. (1)]. The high spatial resolution of the hydrophone was exploited to map the velocity field in the  $(x, z)$  plane from pressure gradients. Figure 1(c) shows the normalized map of the transverse acoustic spin density component  $s_y$

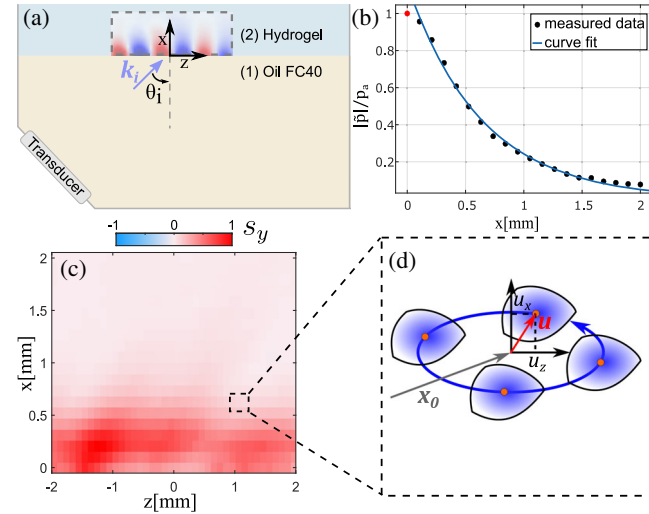


FIG. 1. (a) Setup to generate an evanescent field by supercritical reflection at the interface of two media (inset: experimental pressure field propagating along  $z$ ). (b) Exponential decay of the amplitude along  $x$ . (c) Transverse spin AM density  $s_y$  generated by the evanescent wave (normalized). (d) Schematic representation of the periodic elliptical motion of a fluid particle about its position at rest  $\mathbf{x}_0$ .

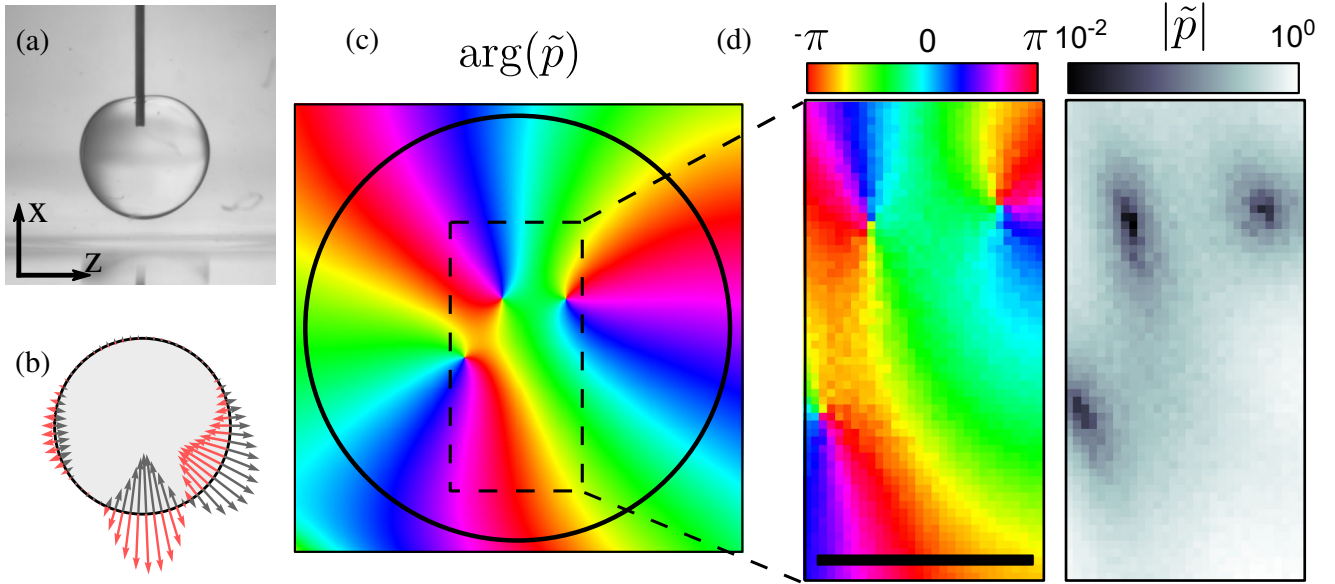


FIG. 2. (a) Photograph of a droplet positioned near the interface with the inserted hydrophone. (b) Normal projections of the modeled incident velocity field forcing the droplet at  $t = 0.2/f$  (gray) and  $t = 0.7/f$  (red). (c) Numerical phase field,  $\arg(\tilde{p})$  inside and outside of the droplet ( $a = 1.12$  mm and  $f = 0.54$  MHz). (d) Experimental phase and magnitude (logarithmic scale) of the pressure field  $\tilde{p}$ . Scale bar represents  $500$   $\mu\text{m}$ .

generated by the evanescent wave. The handedness of the elliptical motion is set by the wave propagation direction (increasing  $z$ ) and constrains the spin density  $s_y$  to be positive.

*Confined phase singularities in a resonant droplet.*—Let us now illustrate how the incident inhomogeneous wave couples with an isolated object. A single fluorinated oil droplet of radius  $a$  was directly injected using a syringe in medium (2) [Fig. 2(a)]. The carbomer concentration composing the hydrogel was sufficiently high to maintain in place droplets ranging in size from a few hundred microns to several millimeters, but remained low enough to preserve propagation characteristics similar to those of water. This strategy has previously been proposed to trap gas bubbles [45]. A first droplet of radius  $a = 1.12$  mm was positioned at a distance roughly equal to the incident wave's decay length  $1/\kappa$  from the interface to ensure a strong and detectable interaction. Furthermore, the large acoustic contrast between the droplet and medium (2) favors the existence of large amplitude Mie-type scattering resonances that we exploited [46]. Calculations of the resulting acoustic field inside and outside of the droplet were obtained using a semianalytical scattering model described elsewhere [47]. All numerical and experimental results are shown in the  $(z, x)$  plane for  $y = 0$ . The center of the droplet is positioned at  $x = y = z = 0$  in the calculations.

Figure 2(b) shows a numerical projection of the incident velocity field normal to the droplet surface. The elliptical fluid motion characterizing the inhomogeneous incident wave in the outer fluid has the ability to generate nonzero normal velocity components on the lower hemisphere of

the droplet. It is important to note that normal velocity components also force the upper hemisphere, but are much weaker in amplitude due to the evanescent nature of the incident field. Consequently, in clear contrast with a situation for which a droplet would be forced by a locally homogeneous ( $z$  axisymmetric) wave front, here the internal acoustic field is imparted with a progressive wave front circulating anticlockwise around the droplet center, from the lower hemisphere where it is generated, toward the upper hemisphere. This is evidenced by the spatial properties of the wave's phase shown in Figs. 2(c) and 2(d), for the droplet forced on its hexapolar resonant mode (for  $f = 0.54$  MHz or  $ka \sim 2.55$ ). The numerical phase map [Fig. 2(c)] shows a particular variation pattern around a circular path around the droplet center close to the drop periphery. More precisely, we observe three phase ramps from  $-\pi$  to  $\pi$  around three points where the phase is undefined. These specific locations in space, known as phase singularities, are well documented for wave fields propagating in free space [48], which include the important class of acoustical and optical vortex beams [21,22,49–51]. In the present case, however, the singularities are *confined* within the resonant structure, and though we note similar phase singularities should naturally emerge in optical waveguides or resonators, there are, to our knowledge, only a few experiments that have succeeded in detecting such phase topologies [52]. Here, to experimentally detect these singular regions, we maneuvered the hydrophone through the droplet's interface while inducing a limited capillary distortion [Fig. 2(a)]. The region we managed to map inside the immobilized droplet was approximately  $500$   $\mu\text{m}$  wide and  $1.2$  mm high. The phase and magnitude

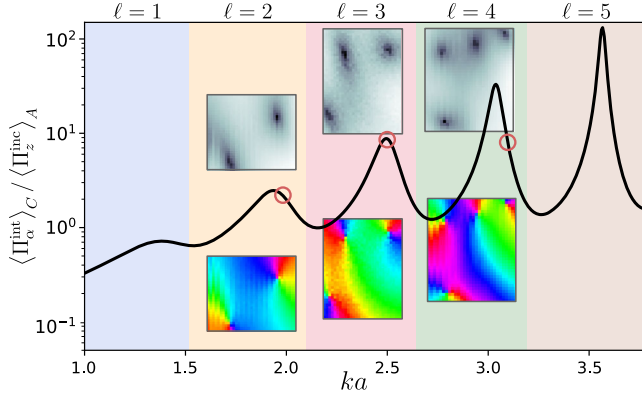


FIG. 3. Curve: modeled average angular energy flux of the internal wave  $\langle \Pi_{\alpha}^{\text{int}} \rangle_C$  normalized by the average incident energy flux  $\langle \Pi_z^{\text{inc}} \rangle_A$ . Colored regions in  $ka$  space correspond to integer values of the total topological charge  $\ell$  calculated for the numerical internal field. Insets: experimental phase and magnitude maps of the internal pressure field measured for  $ka$  values equal to 1.9, 2.55, and 3.18, and indicated by red circles on the resonance curve. The pixel size is approximately  $30 \mu\text{m}$ .

of the field were retrieved from the instantaneous pressure measurements [Fig. 2(d)], and confirm the existence of the confined phase singularities.

To further explore the relationship between droplet size, frequency, and phase topology, we investigated other properties of the internal wave. The energy flux, or Poynting vector, is defined as  $\mathbf{\Pi} = p\mathbf{v}$ , where  $p$  and  $\mathbf{v}$  can refer to the pressure and velocity fields of either the incident or internal wave fields. Figure 3 shows a calculation of the angular component of the energy flux carried by the internal field,  $\langle \Pi_{\alpha}^{\text{int}} \rangle_C$ , which has been normalized by the energy flux carried by the incident wave along the propagation direction,  $\langle \Pi_z^{\text{inc}} \rangle_A$ . The latter was averaged over the cross-section  $A = \pi a^2$  orientated perpendicular to

$z$ , whereas the internal angular energy flux was averaged over the circular path  $C = 2\pi a$  with an angle  $\alpha$  defined between the horizontal and vertical axes passing through the droplet center, and varying from  $0$  to  $2\pi$ . Doing so, the circulating energy flux reveals clear amplification peaks coinciding with the resonant modes of the droplet. Remarkably, each peak is located in regions of  $ka$ -space characterized by an integer value of the total topological charge defined as  $\ell = 1/2\pi \oint_C d\chi$ , where  $\chi = \arg(\tilde{p})$  [53]. The insets in Fig. 3 show experimental phase and magnitude maps that we were able to measure exploiting the position stability of two other droplets and the bandwidth of the transducer (see Supplemental Material [39]). Our summarized measurements for the approximate values  $ka = 1.9, 2.55,$  and  $3.18$  unambiguously show that the integer total topological charge  $\ell$  originates from  $\ell$  coexisting, but not colocalized, phase singularities of topological charge 1, and coincides with the resonance order of the droplet, i.e., quadrupolar ( $\ell = 2$ ), hexapolar ( $\ell = 3$ ), and octopolar ( $\ell = 4$ ). These locations are regions where the head pulses of the circulating wave front interfere destructively with pulses that were delayed within the incident wave train and interact with the droplet latter. The good timing for these arrivals underpin the appearance of resonance peaks in the angular energy flow  $\langle \Pi_{\alpha}^{\text{int}} \rangle_C$ .

*Spin-to-orbital angular momentum conversion.*—We now analyze the AM density that is imparted to the fluid by the internal wave described in the previous section for the hexapolar mode (topological charge  $\ell = 3$ ). The spin AM density can again be obtained from the highly resolved pressure measurements performed inside the droplet. Remarkably, the spin AM topology inside the droplet is nontrivial [Figs. 4(a)–4(c)]. Its sign changes as the radial distance from the droplet center is increased. This means that, in contrast with the elliptical polarization of the fluid motion characterizing the incident wave [Figs. 1(c) and 1(d)], the

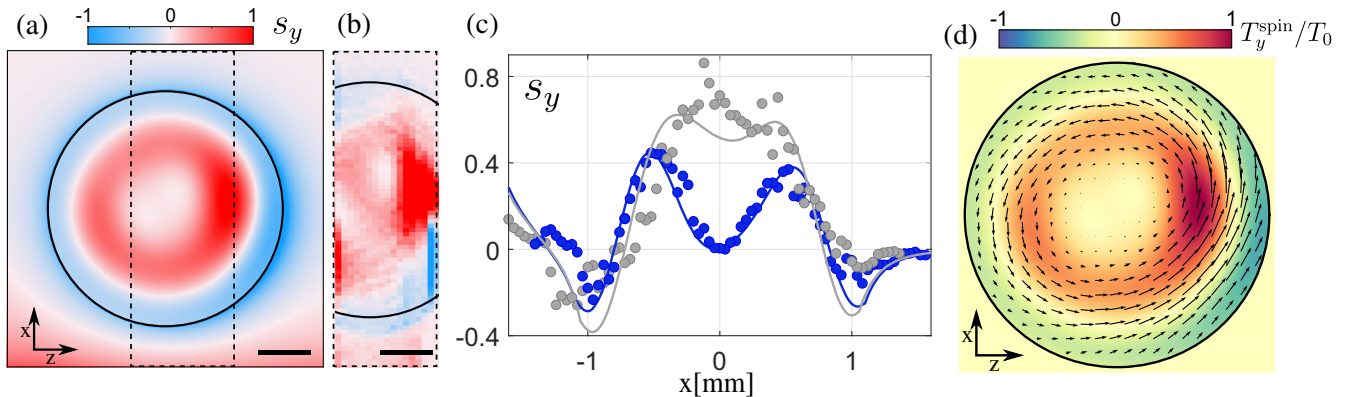


FIG. 4. (a) Numerical spin AM density  $s_y$  obtained for the internal wave shown in Fig. 2 (normalized data and saturated color map). (b) Experimental measurement of the spin AM in the region delimited in (a). Scale bars represent  $500 \mu\text{m}$ . (c) Comparison of experimental and numerical data along two distinct lines traversing the droplet vertically. (d) Acoustic radiation torque  $T_y^{\text{spin}}$  induced on an absorptive probelike particle (normalized by the maximum computed torque  $T_0$ ). Arrows: magnitude of the tangential scattering radiation.

handedness of the polarization inside the droplet can switch from clockwise to anticlockwise in regions of negative and positive spin AM densities, respectively. These oscillations and changes in sign can be better appreciated in Fig. 4(c), where the spin AM density is plotted along two arbitrarily chosen vertical lines traversing the droplet.

Importantly, it is also expected that the circulation of the wave's phase around singularities as described in Figs. 2(c)–2(e) will give rise to a nonzero orbital AM density, in analogy with optical or acoustical vortices [6,22]. According to Ref. [4], the orbital AM density can be computed as  $\mathbf{l} = \mathbf{r} \times \mathbf{p}$ , where  $\mathbf{p} = (\rho/2\omega)\text{Im}[\mathbf{v}^* \cdot (\nabla)\mathbf{v}]$  is the canonical momentum density of the internal wave, and  $\mathbf{r}$  the position vector whose origin is the droplet center. To quantify the AM conversion between the spin-carrying incident wave and the internal circulating hexapolar mode, we computed the integral values of the spin and orbital AM densities generated inside the droplet volume from the numerical data. The orbital AM to spin ratio of their integral values is approximately equal to 92%, meaning most of the AM exists in its orbital form, confirming an efficient transfer of momentum to the internal circulating mode. We additionally found that this ratio remains similar for the other resonant modes.

Finally, we discuss the mechanical effects that would be induced by the two distinctive forms of AM on an absorptive probe particle placed inside the droplet. For a small subwavelength particle (radius  $a_p \ll \lambda = 2\pi/k_z$ ), a radiation torque will be exerted and has been related in Ref. [33] to the local value of the transverse spin density by the simple equation,  $T_y^{\text{spin}} = \omega\text{Im}(\alpha_d)s_y$ , where  $\alpha_d$  is the dipolar polarizability coefficient of the particle (see also Supplemental Material, Sec. II [39] for details on the torque calculation). As seen in Fig. 4(d), the torque's direction is, as expected, directly related to the sign of the spin AM, and the particle would rotate about its own axis clockwise or anticlockwise, depending on its position within the droplet. Simultaneously, the orbital AM is associated with a scattering radiation force,  $\mathbf{F}^{\text{scat}}$ , or alternatively a scattering radiation torque  $T_y^{\text{scat}}$ , about the  $y$  axis passing through the drop center (Supplemental Material, Sec. II [39]), that accelerates the particle. The tangential component of the force is represented by arrows in Fig. 4(d), and suggests the particle will be set on an anticlockwise orbital trajectory around the droplet center. We find that at the position maximizing  $T_y^{\text{spin}}$ , the ratio between both torques  $T_y^{\text{scat}}/T_y^{\text{spin}}$  approximates 91%, consistent with the dominant fraction of orbital AM in the droplet.

*Conclusion and perspectives.*—Our results suggest that the conversion of AM between its spin and orbital form may be very common when an inhomogeneous wave front interacts with targets of simple geometrical forms, impinging a clear acoustic signature to the internal field: the presence of phase singularities. This Letter also shows that complex spin “textures” can be accurately measured in

space, and therefore prepares for further investigations on the central role the spin AM density can have in inducing mechanical rotation, a role that has to date been overlooked in previous studies [23,24,54,55]. Extending the field analysis to objects having other geometries, or with passive [56] or active [57] “chiral” scattering properties could also reveal other routes to the conversion of angular momentum.

Several applications including acoustic imaging and sensing, particle manipulation [55,58–60], or developing devices for chiral wave guiding [25–28,61] are expected to benefit from a better understanding of the AM properties of sound waves.

---

\*diego.baresch@u-bordeaux.fr

- [1] Y. Long, J. Ren, and H. Chen, Intrinsic spin of elastic waves, *Proc. Natl. Acad. Sci. U.S.A.* **115**, 9951 (2018).
- [2] C. Shi, R. Zhao, Y. Long, S. Yang, Y. Wang, H. Chen, J. Ren, and X. Zhang, Observation of acoustic spin, *Natl. Sci. Rev.* **6**, 707 (2019).
- [3] K. Y. Bliokh and F. Nori, Transverse spin and surface waves in acoustic metamaterials, *Phys. Rev. B* **99**, 020301(R) (2019).
- [4] K. Y. Bliokh and F. Nori, Spin and orbital angular momenta of acoustic beams, *Phys. Rev. B* **99**, 174310 (2019).
- [5] R. A. Beth, Mechanical detection and measurement of the angular momentum of light, *Phys. Rev.* **50**, 115 (1936).
- [6] L. Allen, M. W. Beijersbergen, R. J. C. Spreeuw, and J. P. Woerdman, Orbital angular momentum of light and the transformation of Laguerre-Gaussian laser modes, *Phys. Rev. A* **45**, 8185 (1992).
- [7] N. Simpson, K. Dholakia, and M. Padgett, Mechanical equivalence of spin and orbital angular momentum of light: An optical spanner, *Opt. Lett.* **22**, 52 (1997).
- [8] A. T. O’neil, I. MacVicar, L. Allen, and M. J. Padgett, Intrinsic and Extrinsic Nature of the Orbital Angular Momentum of a Light Beam, *Phys. Rev. Lett.* **88**, 053601 (2002).
- [9] M. Padgett, S. Barnett, and R. Loudon, The angular momentum of light inside a dielectric, *J. Mod. Opt.* **50**, 1555 (2003).
- [10] K. Y. Bliokh, A. Y. Bekshaev, and F. Nori, Extraordinary momentum and spin in evanescent waves, *Nat. Commun.* **5**, 1 (2014).
- [11] M. Neugebauer, T. Bauer, A. Aiello, and P. Banzer, Measuring the Transverse Spin Density of Light, *Phys. Rev. Lett.* **114**, 063901 (2015).
- [12] K. Y. Bliokh, F. J. Rodríguez-Fortuño, F. Nori, and A. V. Zayats, Spin-orbit interactions of light, *Nat. Photonics* **9**, 796 (2015).
- [13] Y. Zhao, J. S. Edgar, G. D. M. Jeffries, D. McGloin, and D. T. Chiu, Spin-to-Orbital Angular Momentum Conversion in a Strongly Focused Optical Beam, *Phys. Rev. Lett.* **99**, 073901 (2007).
- [14] K. Y. Bliokh, E. A. Ostrovskaya, M. A. Alonso, O. G. Rodríguez-Herrera, D. Lara, and C. Dainty, Spin-to-orbital

- angular momentum conversion in focusing, scattering, and imaging systems, *Opt. Express* **19**, 26132 (2011).
- [15] M. F. Andersen, C. Ryu, P. Cladé, V. Natarajan, A. Vaziri, K. Helmerson, and W. D. Phillips, Quantized Rotation of Atoms from Photons with Orbital Angular Momentum, *Phys. Rev. Lett.* **97**, 170406 (2006).
- [16] R. Mitsch, C. Sayrin, B. Albrecht, P. Schneeweiss, and A. Rauschenbeutel, Exploiting the local polarization of strongly confined light for sub-micrometer-resolution internal state preparation and manipulation of cold atoms, *Phys. Rev. A* **89**, 063829 (2014).
- [17] M. Hayes, Inhomogeneous plane waves, in *The Breadth and Depth of Continuum Mechanics* (Springer, New York, 1986), pp. 247–285.
- [18] M. Deschamps and B. Hosten, Génération de l'onde hétérogène de volume dans un liquide non absorbant, *Acta Acust. Acust.* **68**, 92 (1989).
- [19] K. Y. Bliokh, M. A. Alonso, D. Sugic, M. Perrin, F. Nori, and E. Brasselet, Polarization singularities and möbius strips in sound and water-surface waves, *Phys. Fluids* **33**, 077122 (2021).
- [20] R. D. Muelas-Hurtado, K. Volke-Sepúlveda, J. L. Ealo, F. Nori, M. A. Alonso, K. Y. Bliokh, and E. Brasselet, Observation of Polarization Singularities and Topological Textures in Sound Waves, *Phys. Rev. Lett.* **129**, 204301 (2022).
- [21] B. T. Hefner and P. L. Marston, An acoustical helicoidal wave transducer with applications for the alignment of ultrasonic and underwater systems, *J. Acoust. Soc. Am.* **106**, 3313 (1999).
- [22] J.-L. Thomas and R. Marchiano, Pseudo Angular Momentum and Topological Charge Conservation for Non-linear Acoustical Vortices, *Phys. Rev. Lett.* **91**, 1 (2003).
- [23] K. Volke-Sepúlveda, A. O. Santillán, and R. R. Boulosa, Transfer of Angular Momentum to Matter from Acoustical Vortices in Free Space, *Phys. Rev. Lett.* **100**, 024302 (2008).
- [24] A. Anhäuser, R. Wunenburger, and E. Brasselet, Acoustical Rotational Manipulation Using Orbital Angular Momentum Transfer, *Phys. Rev. Lett.* **109**, 034301 (2012).
- [25] C. He, X. Ni, H. Ge, X.-C. Sun, Y.-B. Chen, M.-H. Lu, X.-P. Liu, and Y.-F. Chen, Acoustic topological insulator and robust one-way sound transport, *Nat. Phys.* **12**, 1124 (2016).
- [26] H. Ge, X.-Y. Xu, L. Liu, R. Xu, Z.-K. Lin, S.-Y. Yu, M. Bao, J.-H. Jiang, M.-H. Lu, and Y.-F. Chen, Observation of Acoustic Skyrmions, *Phys. Rev. Lett.* **127**, 144502 (2021).
- [27] X.-D. Fan and L. Zhang, Acoustic orbital angular momentum Hall effect and realization using a metasurface, *Phys. Rev. Res.* **3**, 013251 (2021).
- [28] S. Wang, G. Zhang, X. Wang, Q. Tong, J. Li, and G. Ma, Spin-orbit interactions of transverse sound, *Nat. Commun.* **12**, 6125 (2021).
- [29] A. T. Levine, A note concerning the spin of the phonon, *Nuovo Cimento (1955–1965)* **26**, 190 (1962).
- [30] A. McLellan, Angular momentum states for phonons and a rotationally invariant development of lattice dynamics, *J. Phys. C* **21**, 1177 (1988).
- [31] L. Zhang and Q. Niu, Angular Momentum of Phonons and the Einstein–de Haas Effect, *Phys. Rev. Lett.* **112**, 085503 (2014).
- [32] J. Holanda, D. Maior, A. Azevedo, and S. Rezende, Detecting the phonon spin in magnon–phonon conversion experiments, *Nat. Phys.* **14**, 500 (2018).
- [33] I. D. Toftul, K. Y. Bliokh, M. I. Petrov, and F. Nori, Acoustic Radiation Force and Torque on Small Particles as Measures of the Canonical Momentum and Spin Densities, *Phys. Rev. Lett.* **123**, 183901 (2019).
- [34] J. H. Lopes, E. B. Lima, J. P. Leão-Neto, and G. T. Silva, Acoustic spin transfer to a subwavelength spheroidal particle, *Phys. Rev. E* **101**, 043102 (2020).
- [35] W. L. Jones, Asymmetric wave-stress tensors and wave spin, *J. Fluid Mech.* **58**, 737 (1973).
- [36] K. Y. Bliokh, H. Punzmann, H. Xia, F. Nori, and M. Shats, Field theory spin and momentum in water waves, *Sci. Adv.* **8**, eabm1295 (2022).
- [37] C. F. Osterhoudt, D. B. Thiessen, S. F. Morse, and P. L. Marston, Evanescent acoustic waves from subcritical beam illumination: Laboratory measurements near a liquid-liquid interface, *IEEE Journal of Oceanic Engineering* **33**, 397 (2008).
- [38] D. S. Plotnick, T. M. Marston, and P. L. Marston, Circular synthetic aperture sonar imaging of simple objects illuminated by an evanescent wave field, *J. Acoust. Soc. Am.* **140**, 2839 (2016).
- [39] See Supplemental Material at <http://link.aps.org/supplemental/10.1103/PhysRevLett.131.114001> for additional information on the experimental setup and radiation force and torque calculations, and citations of Refs. [40–43].
- [40] P. Lidon, L. Villa, and S. Manneville, Power-law creep and residual stresses in a carbopol gel, *Rheol. Acta* **56**, 307 (2017).
- [41] M. Settnes and H. Bruus, Forces acting on a small particle in an acoustical field in a viscous fluid, *Phys. Rev. E* **85**, 016327 (2012).
- [42] J. T. Karlsen and H. Bruus, Forces acting on a small particle in an acoustical field in a thermoviscous fluid, *Phys. Rev. E* **92**, 043010 (2015).
- [43] D. Baresch, J.-L. Thomas, and R. Marchiano, Three-dimensional acoustic radiation force on an arbitrarily located elastic sphere, *J. Acoust. Soc. Am.* **133**, 25 (2013).
- [44] B. Tallon, T. Brunet, and J. H. Page, Impact of Strong Scattering Resonances on Ballistic and Diffusive Wave Transport, *Phys. Rev. Lett.* **119**, 164301 (2017).
- [45] V. Leroy, A. Strybulevych, J. H. Page, and M. G. Scanlon, Sound velocity and attenuation in bubbly gels measured by transmission experiments, *J. Acoust. Soc. Am.* **123**, 1931 (2008).
- [46] T. Brunet, S. Raffy, B. Mascaro, J. Leng, R. Wunenburger, O. Mondain-Monval, O. Poncelet, and C. Aristégui, Sharp acoustic multipolar-resonances in highly monodisperse emulsions, *Appl. Phys. Lett.* **101**, 011913 (2012).
- [47] L. Alhaïtz, D. Baresch, T. Brunet, C. Aristégui, and O. Poncelet, Spiral-shaped scattered field from incident evanescent acoustic waves on a Mie particle, in *Journal of Physics: Conference Series* (IOP Publishing, 2021), Vol. 1761, p. 012003, [10.1088/1742-6596/1761/1/012003](https://doi.org/10.1088/1742-6596/1761/1/012003).
- [48] J. Nye and M. Berry, Dislocations in wave trains, *Proc. R. Soc. A* **336**, 165 (1974).

- [49] P. Couillet, L. Gil, and F. Rocca, Optical vortices, *Opt. Commun.* **73**, 403 (1989).
- [50] M. S. Soskin, V. N. Gorshkov, M. V. Vasnetsov, J. T. Malos, and N. R. Heckenberg, Topological charge and angular momentum of light beams carrying optical vortices, *Phys. Rev. A* **56**, 4064 (1997).
- [51] A. M. Yao and M. J. Padgett, Orbital angular momentum: Origins, behavior and applications, *Adv. Opt. Photonics* **3**, 161 (2011).
- [52] M. L. M. Balistreri, J. P. Korterik, L. Kuipers, and N. F. Van Hulst, Local Observations of Phase Singularities in Optical Fields in Waveguide Structures, *Phys. Rev. Lett.* **85**, 294 (2000).
- [53] M. R. Dennis, K. O'holleran, and M. J. Padgett, Singular optics: Optical vortices and polarization singularities, in *Progress in Optics* (Elsevier, New York, 2009), Vol. 53, pp. 293–363.
- [54] K. D. Skeldon, C. Wilson, M. Edgar, and M. J. Padgett, An acoustic spanner and its associated rotational Doppler shift, *New J. Phys.* **10**, 013018 (2008).
- [55] D. Baresch, J.-L. Thomas, and R. Marchiano, Orbital angular momentum transfer to stably trapped elastic particles in acoustical vortex beams, *Phys. Rev. Lett.* **121**, 074301 (2018).
- [56] R. Wunenburger, J. I. V. Lozano, and E. Brasselet, Acoustic orbital angular momentum transfer to matter by chiral scattering, *New J. Phys.* **17** (2015).
- [57] H. Nassar, B. Yousefzadeh, R. Fleury, M. Ruzzene, A. Alù, C. Daraio, A. N. Norris, G. Huang, and M. R. Haberman, Nonreciprocity in acoustic and elastic materials, *Nat. Rev. Mater.* **5**, 667 (2020).
- [58] D. Baresch, J.-L. Thomas, and R. Marchiano, Observation of a Single-Beam Gradient Force Acoustical Trap for Elastic Particles: Acoustical Tweezers, *Phys. Rev. Lett.* **116**, 024301 (2016).
- [59] A. Marzo, M. Caleap, and B. W. Drinkwater, Acoustic Virtual Vortices with Tunable Orbital Angular Momentum for Trapping of Mie Particles, *Phys. Rev. Lett.* **120**, 044301 (2018).
- [60] H. Bruus, J. Dual, J. Hawkes, M. Hill, T. Laurell, J. Nilsson, S. Radel, S. Sadhal, and M. Wiklund, Forthcoming lab on a chip tutorial series on acoustofluidics: Acoustofluidics—Exploiting ultrasonic standing wave forces and acoustic streaming in microfluidic systems for cell and particle manipulation, *Lab Chip* **11**, 3579 (2011).
- [61] M. Lanoy, F. Lemoult, A. Eddi, and C. Prada, Dirac cones and chiral selection of elastic waves in a soft strip, *Proc. Natl. Acad. Sci. U.S.A.* **117**, 30186 (2020).